# Effects of Surface Shape on the Geometry and Surface Topography of the Melt Pool in Low-Power Density Laser Melting

**Young-Deuk Kim**
Dept. of Mechanical Engineering, Hanyang University, 17 Haengdang-dong, Seongdong-gu, Seoul 133-791,
Republic of Korea

**Woo-Seung Kim**
Dept. of Mechanical Engineering, Hanyang University, 1271 Sa 3-dong, Sangnok-gu, Ansan, Gyeonggi-do 426-791,
Republic of Korea

*DOI 10.1002/aic.12620*

*The quantitative correlations between workpiece volume and melt pool geometry, as well as the flow and thermal features of the melt pool are established. Thermocapillary convections in melt pool with a deformable free surface are investigated with respect to surface shape and laser intensity. When the contact angle between the tangent to the top surface and the vertical wall at the hot center is acute, the free surface flattens, compared with that of the initial free surface. Otherwise, the free surface forms a bowl-like shape with a deep crater and a low peripheral rim when the contact angle at the hot center is obtuse. Increasing the workpiece volume at a fixed laser intensity and a negative radial height gradient cause linear decreases in the geometric size and magnitude of flow and temperature of the melt pool. Conversely, linear increases are observed with a positive radial height gradient.* © 2011 American Institute of Chemical Engineers *AIChE J,* 58: 998–1011, 2012

*Keywords: laser melting, free surface flow, thermocapillary convection, curved free surface, surface topography, numerical analysis*

## Introduction

Laser-assisted melting and surface modification processes are important in a variety of industrial applications. In the laser surface melting process, the thermal behavior and fluid flow of the melt pool significantly affect its shape, size, and surface topography (bumps). The fluid flow in the melt pool is driven primarily by the spatial variation in its surface tension, caused by the large temperature gradient. Therefore, many experimental and numerical studies have been conducted to investigate the heat and fluid flow characteristics of the melt pools formed during laser processing of various materials. All of these studies are based on the process parameters, such as laser power intensity, relative laser source-workpiece velocity (scanning velocity), shape and dimensions of the workpiece area on which the laser beam impinges (laser spot), laser beam mode and intensity cross-sectional distribution, and beam geometry.[1]

The transient surface deformations of Ni-P disk substrates and metallic thin films upon pulsed laser heating have been examined experimentally.[2–5] Several different surface shapes have been found (V-type bump, sombrero bump, and double-rim bump), resulting from different pulse energies of the laser beam. With a nondeformable flat surface, many

---

Correspondence concerning this article should be addressed to W.-S. Kim at wskim@hanyang.ac.kr.
Current Address of Young-Deuk Kim: Water Desalination and Reuse Center, 4700 King Abdullah University of Science and Technology, Thuwal 23955-6900, Saudi Arabia.

numerical analyses have been performed to investigate the thermal behaviors and fluid flows in the molten pools as a function of various laser process parameters.[6–17] Prior studies have shown that buoyancy forces in the molten pool can be neglected,[9] and the scanning velocity is insignificant because of the higher magnitude of the surface tension-driven velocity.[9,10] In addition, in the laser material interaction process with a deformable flat surface, the evolution of the melt pool and the dynamic surface deformation were investigated numerically under variable process parameters, including with various materials and thermophysical properties of the substrate, laser beam intensities, intensity distributions, and scanning speeds.[18–24] Ha and Kim[21] and Han et al.[22] show that an assumption of a flat free surface causes an apparent discrepancy between the predicted melt pool geometry and the real situation. In our previous work,[24] we considered the effect of the surface shape of the substrate on the geometry and surface topography of the melt pool using the intensity distribution of the Gaussian laser beam. It was found that variation in the substrate surface shape significantly affects the shape, size, and surface deformation of the melt pool. However, that work focused only on a workpiece with an obtuse contact angle between the tangent to the free surface and the vertical cylinder wall at the hot center. A limited number of numerical simulations have been reported on thermocapillary convection in laser surface melting processes with a deformable flat surface compared with the reported cases with a nondeformable flat surface. In particular, no detailed numerical analyses on the geometry and surface topography of the melt pool in laser-assisted melting with various curved surface shapes have been discussed in previous research.

This study, therefore, focuses on the establishment of quantitative correlations between workpiece volume and melt pool geometry (width, depth, aspect ratio, and volume of the melt pool), as well as the flow (maximum stream function and surface velocity) and thermal (maximum surface temperature) features in the melt pool for various surface shapes at a fixed laser intensity. In the present work, prior to solving the laser melting problems, axisymmetric, two-dimensional numerical simulations are carried out to examine the effect of the free surface shapes on the flow characteristics of thermocapillary convection in an open cylinder with a nondeformable free surface at a fixed liquid volume. The effect of the surface shapes on the shape, size, and surface topography of the melt pool is then investigated via axisymmetric, two-dimensional numerical analyses of the laser surface melting processes with a deformable free surface for various curved surface shapes. To demonstrate the linearity of the geometrical, flow, and thermal features of the melt pool depending on the workpiece volume obtained at a fixed laser intensity, we analyze thermocapillary convection during laser melting for various surface shapes under three different low-power laser intensities.

## Model Description

### *Thermocapillary convection in liquid cylinders*

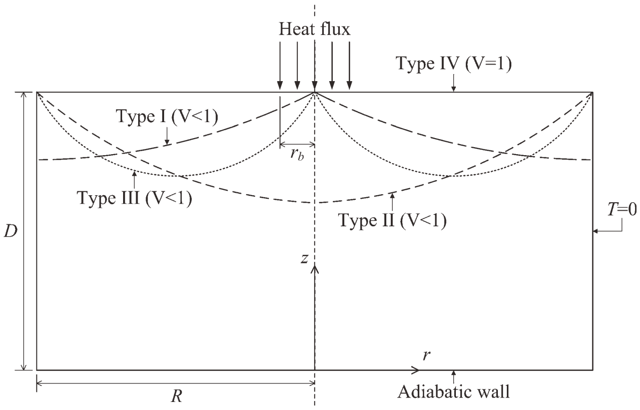

**Figure 1. Schematic illustration of the physical system with various free surface shapes.**

The physical system under consideration is an open cylinder with a flat (Type IV) free surface and three different curved (Types I, II, and III) free surfaces, as shown in Figure 1. The contact angles between the tangent to the free surface and the vertical cylinder wall is acute at the hot center, at the cold corner, and on both sides of the surface shapes of Types I, II, and III, respectively, and these angle decrease with decreasing liquid volume. In the present work, for Types I, II, and III, the thermocapillary convection is analyzed in an open cylinder that has a normalized liquid volume of 0.8 that is filled with an incompressible Newtonian fluid. The free surface is assumed to be nondeformable since the range of the capillary number is much less than unity. An aspect ratio ($R/D$) of 1 and a Prandtl number of 30 are used to compare the numerical predictions with previously published numerical results.[25] A stationary, continuous, axisymmetric laser beam of radius $r_b$ with a uniform heat flux distribution irradiates the surface and the radius of the laser beam is set as 0.1.[25] The vertical wall is maintained at a constant temperature, and the bottom wall is thermally insulated. The surface tension is assumed to be a linear function of temperature

$$\sigma = \sigma_0 - \gamma(T - T_0) \tag{1}$$

With negligible body forces, the nondimensional governing equations are

$$\nabla \cdot \mathbf{v} = 0 \tag{2}$$

$$Re\left(\frac{\partial \mathbf{v}}{\partial t} + \nabla \cdot (\mathbf{v}\mathbf{v})\right) = -\nabla P + \nabla^2 \mathbf{v} \tag{3}$$

$$Ma\left(\frac{\partial T}{\partial t} + \nabla \cdot (\mathbf{v}T)\right) = \nabla^2 \cdot T \tag{4}$$

The length, temperature, velocity, pressure, and time are normalized with respect to $D$, $T_r$, $\gamma T_r/\mu$, $\gamma T_r/D$, and $\mu HD/\gamma T_r$, respectively.

The boundary conditions considered are

$$u = 0,\ \upsilon = 0,\ T = 0,\ \text{at } r = 1 \tag{5}$$

$$u = 0,\ \upsilon = 0,\ \frac{\partial T}{\partial z} = 0,\ \text{at } z = 0 \tag{6}$$

The nondimensionalized position of the free surface is determined by the function $h(r)$. The thermal, kinematic, and tangential stress balance boundary conditions at the interface ($z = D$) are as follows

$$-\frac{1}{N}\left(h'\frac{\partial T}{\partial r}-\frac{\partial T}{\partial z}\right)=q \tag{7}$$

$$\upsilon = h'u \tag{8}$$

$$\left(1-h'^2\right)\left(\frac{\partial u}{\partial z}+\frac{\partial \upsilon}{\partial r}\right)+2h'\left(\frac{\partial \upsilon}{\partial z}-\frac{\partial u}{\partial r}\right)=-N\left(\frac{\partial T}{\partial r}+h'\frac{\partial T}{\partial z}\right) \tag{9}$$

where $q = 1/H_r^2$ at $r \le H_r$ and $q = 0$ at $r > H_r$, $H_r = r_b/R$, $N = \left(1+h'^2\right)^{1/2}$, and $h' = dh/dr$.

The shape of the interface can be determined by Eq. 10 and the liquid volume Eq. 11 with a given liquid volume. Eq. 10 is derived from the Young-Laplace equation, obtained by simplifying the normal stress balance equation with an assumption to neglect the dynamic surface deformation at $Ca \ll 1$[26] and two boundary conditions, $h'(0) = 0$ and $h(1) = 1$. These equations are as follows

$$h(r)=1+\frac{1}{C}\left[\left(1-C^2\right)^{1/2}-\left(1-C^2r^2\right)^{1/2}\right] \tag{10}$$

$$V = 2\int_0^1 rh\mathrm{d}r \tag{11}$$

where $C = -Ca\Delta P/2$. $\Delta P = P - P_0$ is the nondimensional pressure difference between the interface liquid and the gas pressures, where the liquid volume is normalized with respect to $\pi R^2 D$.

In the present work, however, to examine the influence of the free surface shape on the thermocapillary convection, as shown in Figure 1, the four types of free surface shapes are generated using the following equations instead of solving the Young-Laplace equation. These shapes are defined as follows

$$h(r) = a(r-1)^2+b \text{ with } h(0) = 1,\ \text{for Type I;} \tag{12}$$

$$h(r) = ar^2+b \text{ with } h(1) = 1,\ \text{for Type II;} \tag{13}$$

$$h(r) = a(r-0.5)^2+b \text{ with } h(0) = 1 \text{ and } h(1) = 1,\ \text{for Type III;} \tag{14}$$

$$h(r) = 1,\ \text{for Type IV} \tag{15}$$

As shown in Eqs. 12–15, the free surface is pinned at the top edge of the hot center, at the cold wall, and on both sides, for the surface shapes of Types I, II, and III, respectively. If the liquid volume is given, the constants $a$ and $b$ and the shape of the interface $h(r)$ are determined by Eqs. 11–15.

To solve the problem with a curved surface, the physical domain ($r$, $z$) is mapped onto a rectangular computational domain ($\xi$, $\eta$), where

$$\xi = r \tag{16}$$

$$\eta = \frac{z}{h(r)} \tag{17}$$

The governing equations transformed into the computational domain are

$$\frac{1}{\xi}\frac{\partial \xi u}{\partial \xi}-\eta\frac{h'}{h}\frac{\partial u}{\partial \eta}+\frac{1}{h}\frac{\partial \upsilon}{\partial \eta}=0 \tag{18}$$

$$Re\left[\frac{\partial u}{\partial t}+\frac{1}{\xi}\frac{\partial \xi u^2}{\partial \xi}-\eta\frac{h'}{h}\frac{\partial u^2}{\partial \eta}+\frac{1}{h}\frac{\partial u\upsilon}{\partial \eta}\right] = -\frac{\partial P}{\partial \xi}+\eta\frac{h'}{h}\frac{\partial P}{\partial \eta}-\frac{u}{\xi^2}+\nabla^2 u \tag{19}$$

$$Re\left[\frac{\partial \upsilon}{\partial t}+\frac{1}{\xi}\frac{\partial \xi u\upsilon}{\partial \xi}-\eta\frac{h'}{h}\frac{\partial u\upsilon}{\partial \eta}+\frac{1}{h}\frac{\partial \upsilon^2}{\partial \eta}\right]=-\frac{1}{h}\frac{\partial P}{\partial \eta}+\nabla^2\upsilon \tag{20}$$

$$PrRe\left[\frac{\partial T}{\partial t}+\frac{1}{\xi}\frac{\partial \xi uT}{\partial \xi}-\eta\frac{h'}{h}\frac{\partial uT}{\partial \eta}+\frac{1}{h}\frac{\partial \upsilon T}{\partial \eta}\right]=\nabla^2 T \tag{21}$$

$$\nabla^2=\frac{1}{\xi}\frac{\partial}{\partial \xi}\left(\xi\frac{\partial}{\partial \xi}\right)-\frac{2\eta h'}{h}\frac{\partial^2}{\partial\eta\partial\xi} +\left[2\left(\frac{h'}{h}\right)^2-\frac{h''}{h}-\frac{h'}{h\xi}\right]\eta\frac{\partial}{\partial \eta}+\left[\left(\frac{\eta h'}{h}\right)^2+\frac{1}{h^2}\right]\frac{\partial^2}{\partial \eta^2} \tag{22}$$

The transformed boundary conditions become

$$\text{At } \xi = 1,\ u = 0,\ \upsilon = 0,\ T = 0 \tag{23}$$

$$\text{At } \eta = 0,\ u = 0,\ \upsilon = 0,\ \frac{\partial T}{\partial \eta} = 0 \tag{24}$$

At the interface ($\eta = 1$),

$$\frac{(1+h'^2)}{h}\frac{\partial T}{\partial \eta}-h'\frac{\partial T}{\partial \xi}=Nq \tag{25}$$

$$\upsilon = h'u \tag{26}$$

$$\left(\frac{1+h'^2}{h}\right)\frac{\partial u}{\partial \eta}-2h'\frac{\partial u}{\partial \xi}+\left(\frac{h'+h'^3}{h}\right)\frac{\partial \upsilon}{\partial \eta} +\left(1-h'^2\right)\frac{\partial \upsilon}{\partial \xi}=-N\frac{\partial T}{\partial \xi} \tag{27}$$

The free surface shape $h(r)$ with a given liquid volume is determined by Eqs. 11–15 using Broyden's method, a quasi-Newtonian method to find the numerical solution to nonlinear equations.[27] The transformed governing Eqs. 18–21 and boundary conditions Eqs. 23–27 are solved using a finite volume method employing a SIMPLER algorithm. Nonuniform grids are constructed with a finer mesh of $81(r) \times 81(z)$ in the regions near the free surface and at the bottom and side walls where the boundary layers develop. Convergence criteria for iterations within a time step or a steady-state are $\left|s^{n+1}-s^n\right|/s^{n+1}<10^{-4}$ and $\left|s^{n+1}-s^n\right|<10^{-10}$, where $s$ is any variable ($u$, $v$, $T$) at all points, and $n$ is the time marching or iteration level. The numerical code is validated by comparing the computed surface temperatures and velocities with those in Sim and Zebib,[25] as

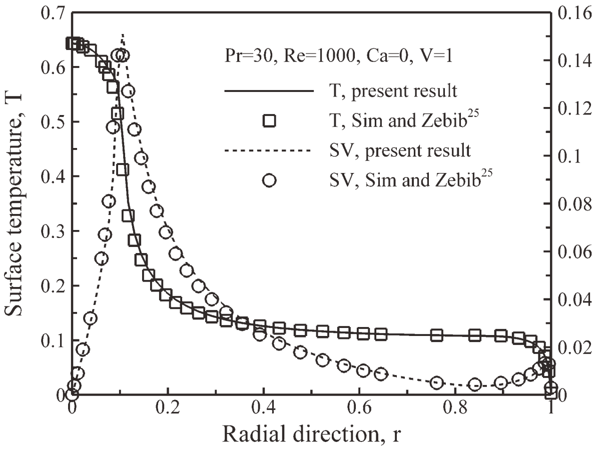

**Figure 2. Surface temperature and velocity distributions with *Re* = 1000, *Pr* = 30, *V* = 1, and $H_r$ = 0.1.**

The calculated results agree well with the numerical results.[25]

shown in Figure 2. The axisymmetric numerical results[25] agreed with the experimental results.[28] The parameters for the simulation are $Pr = 30$, $R/D = 1$, $Ca = 0$, and $Re = 1000$.

### *Laser melting*

A schematic diagram of the physical system considered in this study is shown in Figure 3. A stationary, continuous, axisymmetric laser beam of radius $r_b$ with a Gaussian heat flux distribution irradiates the surface of an opaque material. The aspect ratio of the material and the radius of the laser beam are 1 and 0.5 mm, respectively. Much of the incident radiation is reflected by the heating surface, while the rest is absorbed into the material. The heat absorbed causes the formation of a melt pool, and the flow into the melt pool is driven by surface tension due to a temperature gradient along the free surface or thermocapillary convection. The top surface outside the laser beam is adiabatic, and the bottom and side walls are maintained at a constant temperature, $T_\infty = 300$ K. Surface tension is assumed to be a linear function of temperature.

The nondimensional governing equations for the incompressible fluid flow with negligible body forces and the heat transfer in the melt pool are defined, respectively, as follows

$$\nabla \cdot \mathbf{v} = 0 \tag{28}$$

$$\frac{1}{Ma}\frac{\partial \mathbf{v}}{\partial t} + \nabla \cdot (\mathbf{v}\mathbf{v}) = -\nabla P + \frac{1}{Re}\nabla^2 \mathbf{v} + \mathbf{S} \tag{29}$$

$$\frac{\partial H}{\partial t} + Ma\nabla \cdot (\mathbf{v}H) = \nabla \cdot (k\nabla T) \tag{30}$$

The boundary conditions for solving the governing equations are as follows

$$\frac{\partial T}{\partial r} = u = \frac{\partial \upsilon}{\partial r} = 0, \text{ at } r = 0 \tag{31}$$

$$T = -Ste,\ u = \upsilon = 0, \text{ at } r = 1 \tag{32}$$

$$T = -Ste,\ u = \upsilon = 0, \text{ at } z = 0 \tag{33}$$

The nondimensionalized position of the free surface is described by the function $h(t, r)$. The thermal, kinematic, tangential, and normal stress balance boundary conditions at the gas-liquid interface are

$$\frac{1}{N}\left(-h'\frac{\partial T}{\partial r} + \frac{\partial T}{\partial z}\right) = Bf(r) \tag{34}$$

$$\upsilon = \frac{1}{Ma}\frac{\partial h}{\partial t} + h'u \tag{35}$$

$$\left(1 - h'^2\right)\left(\frac{\partial u}{\partial z} + \frac{\partial \upsilon}{\partial r}\right) + 2h'\left(\frac{\partial \upsilon}{\partial z} - \frac{\partial u}{\partial r}\right) = -N\left(\frac{\partial T}{\partial r} + h'\frac{\partial T}{\partial z}\right) \tag{36}$$

$$-Re \cdot P + \frac{2}{N^2}\left[\frac{\partial \upsilon}{\partial z} + h'^2\frac{\partial u}{\partial r} - h'\left(\frac{\partial \upsilon}{\partial r} + \frac{\partial u}{\partial z}\right)\right] = \frac{1 - Ca \cdot T}{Ca \cdot N}\left(\frac{h''}{N^2} + \frac{h'}{r}\right) \tag{37}$$

where $N = \left(1 + h'^2\right)^{1/2}$, $h' = \partial h/\partial r$, and $Bf(r) = 0$ at $r > 0.5$. As shown in Eq. 37, the free surface curvature is determined by both surface pressure and normal viscous stresses.

In the modeling of laser surface melting, the laser energy has been modeled as either a volumetric heating source for metallic[5–7] and ceramic[8,29,30] materials or a surface heating source for metallic materials.[9–24] It is known that laser absorption length for ceramic materials is several orders of magnitude larger than that of metallic materials.[8] Therefore, a volumetric heating source is more appropriate for modeling the laser energy for laser melting of most ceramic materials.[29,30] In the present work, the energy flux density absorbed by the workpiece surface is determined according to a specified symmetric Gaussian distribution and is given by

$$Bf(r) = \frac{r_b C_p}{k_1 \lambda}\frac{3\phi Q}{\pi r_b^2}\exp\left(-3r^2\right) \tag{38}$$

Here, the absorptivity coefficient $\phi$ is influenced by the natures of the surface state and the surface temperature. In this study, $\phi$ has a value of 0.15.[24]

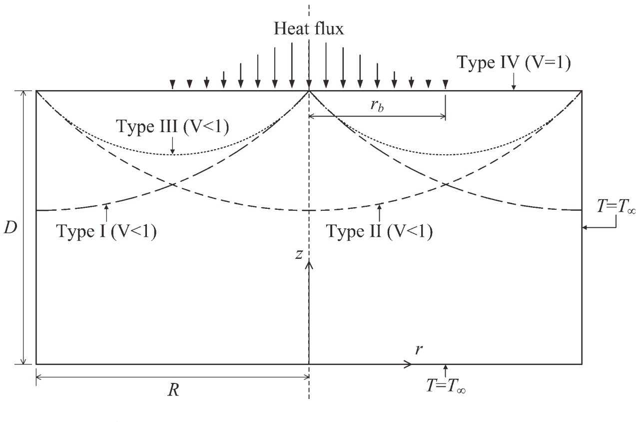

**Figure 3. Schematic illustration of the physical system with various surface shapes.**

The shapes ($h$) of the top surfaces determined by Eqs. 11–15 in a given workpiece volume are used as the initial conditions for solving Eq. 37, and the boundary conditions are:

$$h'(t, r=0) = 0 \tag{39}$$

$$h(t, r=r_{\max}) = h(t=0, r=r_{\max}) \tag{40}$$

Since the liquid volume must satisfy mass conservation, its total volume change should be zero

$$V = \int_0^{r_{\max}} [h(t,r) - h(0,r)] r dr = 0 \tag{41}$$

where $V$ is the nondimensional liquid volume. The nondimensional variables are as follows

$$t = \frac{t^*\alpha}{r_\mathrm{b}^2}, r = \frac{r^*}{r_\mathrm{b}}, \mathbf{v} = \frac{\mathbf{v}^*}{U_\mathrm{R}}, P = \frac{P^*}{\rho U_\mathrm{R}^2}, T = \frac{C_\mathrm{P}(T^* - T_\mathrm{m})}{\lambda}, k = \frac{k^*}{k_1}$$

To solve the laser melting problem for a deformable surface, the physical domain ($t$, $r$, $z$), must be transformed into a rectangular computational domain ($t$, $\xi$, $\eta$), where

$$\xi = r \tag{42}$$

$$\eta = \frac{z}{h(t,r)} \tag{43}$$

The transformed governing equations are

$$\frac{1}{\xi}\frac{\partial \xi u}{\partial \xi} - \eta \frac{h'}{h}\frac{\partial u}{\partial \eta} + \frac{1}{h}\frac{\partial \upsilon}{\partial \eta} = 0 \tag{44}$$

$$\frac{1}{Ma}\left[\frac{\partial u}{\partial t} - \frac{\eta}{h}\frac{\partial h}{\partial t}\frac{\partial u}{\partial \eta}\right] + \frac{1}{\xi}\frac{\partial \xi u^2}{\partial \xi} - \eta\frac{h'}{h}\frac{\partial u^2}{\partial \eta} + \frac{1}{h}\frac{\partial u\upsilon}{\partial \eta} = -\frac{\partial P}{\partial \xi} + \eta\frac{h'}{h}\frac{\partial P}{\partial \eta} + \frac{1}{Re}\left[\nabla^2 u - \frac{u}{\xi^2}\right] + S_u \tag{45}$$

$$\frac{1}{Ma}\left[\frac{\partial \upsilon}{\partial t} - \frac{\eta}{h}\frac{\partial h}{\partial t}\frac{\partial \upsilon}{\partial \eta}\right] + \frac{1}{\xi}\frac{\partial \xi u\upsilon}{\partial \xi} - \eta\frac{h'}{h}\frac{\partial u\upsilon}{\partial \eta} + \frac{1}{h}\frac{\partial \upsilon^2}{\partial \eta} = -\frac{1}{h}\frac{\partial P}{\partial \eta} + \frac{1}{Re}\nabla^2 v + S_v \tag{46}$$

$$\begin{aligned}\frac{\partial T}{\partial t} - \frac{\eta}{h}\frac{\partial h}{\partial t}\frac{\partial T}{\partial \eta} + Ma\left[\frac{1}{\xi}\frac{\partial \xi u T}{\partial \xi} - \eta\frac{h'}{h}\frac{\partial uT}{\partial \eta} - \frac{1}{h}\frac{\partial \upsilon T}{\partial \eta}\right] \\ = \frac{1}{\xi}\frac{\partial}{\partial \xi}\left(k\xi\frac{\partial T}{\partial t}\right) - \frac{\eta h'}{h}\left[\frac{\partial}{\partial \eta}\left(k\frac{\partial T}{\partial \xi}\right) + \frac{\partial}{\partial \xi}\left(k\frac{\partial T}{\partial \eta}\right)\right] \\ + \left[2\left(\frac{h'}{h}\right)^2 - \frac{h''}{h} - \frac{h'}{h\xi}\right]\eta k\frac{\partial T}{\partial \eta} + \left[\left(\frac{h'\eta}{h}\right)^2 + \frac{1}{h^2}\right]\frac{\partial}{\partial \eta}\left(k\frac{\partial T}{\partial \eta}\right) - \frac{\partial f}{\partial t},\end{aligned} \tag{47}$$

$$\nabla^2 = \frac{1}{\xi}\frac{\partial}{\partial \xi}\left(\xi\frac{\partial}{\partial \xi}\right) - \frac{2\eta h'}{h}\frac{\partial^2}{\partial \eta \partial \xi} + \left[2\left(\frac{h'}{h}\right)^2 - \frac{h''}{h} - \frac{h'}{h\xi}\right]\eta\frac{\partial}{\partial \eta} + \left[\left(\frac{\eta h'}{h}\right)^2 + \frac{1}{h^2}\right]\frac{\partial^2}{\partial \eta^2} \tag{48}$$

The momentum and heat transfer on the solid-liquid phase interface is incorporated into the governing equations by introducing appropriate source terms. The source terms $S_u$ and $S_v$ in the momentum Eqs. 45 and 46 depend only on the local liquid fraction $f$. For a liquid control volume without a mushy zone, $f = 1$, while $f = 0$ for a solid. The magnitude of $\mathbf{S}$ in the solid-phase region with $f = 0$ is a large constant ($\approx 10^{10}$), whereas it is zero in the liquid-phase region with $f = 1$. In the energy Eq. 47, the latent heat of fusion is accounted for by the source term,[31] $\frac{\partial f}{\partial t}$.

The transformed boundary conditions become

$$\text{At } \xi = 0,\ \frac{\partial T}{\partial \xi} = u = \frac{\partial \upsilon}{\partial \xi} = 0 \tag{49}$$

$$\text{At } \xi = 1,\ T = -Ste,\ u = \upsilon = 0 \tag{50}$$

$$\text{At } \eta = 0,\ T = -Ste,\ u = \upsilon = 0 \tag{51}$$

At the interface, ($\eta = 1$),

$$\frac{\left(1 + h'^2\right)}{h}\frac{\partial T}{\partial \eta} - h'\frac{\partial T}{\partial \xi} = NBf(\xi) \tag{52}$$

$$\upsilon = \frac{1}{Ma}\frac{\partial h}{\partial t} + h'u \tag{53}$$

$$\left(\frac{1 + h'^2}{h}\right)\frac{\partial u}{\partial \eta} - 2h'\frac{\partial u}{\partial \xi} + \left(\frac{h' + h'^3}{h}\right)\frac{\partial \upsilon}{\partial \eta} + \left(1 - h'^2\right)\frac{\partial \upsilon}{\partial \xi} = -N\frac{\partial T}{\partial \xi} \tag{54}$$

$$-Re \cdot P + \frac{2}{h}\left(\frac{\partial \upsilon}{\partial \eta} - h'\frac{\partial u}{\partial \eta}\right) + \frac{2h'}{N^2}\left(h'\frac{\partial u}{\partial \xi} - \frac{\partial \upsilon}{\partial \xi}\right) = \frac{1 - Ca \cdot T}{Ca \cdot N}\left(\frac{h''}{N^2} + \frac{h'}{\xi}\right) \tag{55}$$

As in Eq. 37, $P$ contains a free integration constant $c(t)$, and the free surface shape, $h(t,r)$, and $c(t)$ are determined using Eqs. 55 and 39–41. Broyden's method[27] is used to determine $c(t)$ at each time.

The free surface shape $h(t,r)$ is unknown and should be obtained as a solution to the coupled governing equations along with the surface force balance. The transformed governing Eqs. 44–47 in conjunction with the boundary conditions Eqs. 49–55 are solved using a finite volume method employing a SIMPLER algorithm. A nonuniform grid system is employed in which the meshes are graded toward the center in the $r$-direction and toward the free surface in the $z$-direction. All computations start with $h(t = 0, r)$, $\mathbf{v} = 0$, and $T = -Ste$. A brief summary of the computational procedure is as follows:

1. Generate the initial top-surface shape using Eqs. 11–15 for the given workpiece volume.
2. Start with initial conditions for $T$, $\mathbf{v}$, and $h$.
3. The rectangular computational domain is generated numerically.
4. Solve the transformed governing Eqs. 44–47 to find $T$ and $\mathbf{v}$ with the transformed boundary conditions in Eqs. 49–54.

**Table 1. Thermophysical Properties of Steel and the Input Parameters for the Simulation[24]**

| Variable | Value | Variable | Value |
|---|---|---|---|
| $\rho$ | 7200 kg m$^{-3}$ | $C_p$ | 753 J kg$^{-1}$ K$^{-1}$ |
| $k_s$ | 31.39 W m$^{-1}$ K$^{-1}$ | $k_1$ | 15.48 W m$^{-1}$ K$^{-1}$ |
| $\mu$ | 0.006 N s m$^{-2}$ | $\lambda$ | $2.47 \times 10^5$ J kg$^{-1}$ |
| $T_m$ | 1723 K | $\gamma$ | $-10^{-6}$ N m$^{-1}$ K$^{-1}$ |
| Process parameters | | | |
| $r_b$ | 0.5 mm | $T_\infty$ | 300 K |
| $Q$ | 400 W, 450 W, 500 W, 600 W, 700 W | $Ca$ | 0.02 |
| $Re$ | 32.8 | $Pr$ | 0.292 |
| $Bf$ (0) | 22.57, 25.39, 28.21, 33.85, 39.49 | $Ste$ | 4.338 |

5. Calculate $h$ and $c$ using the normal stress balance and liquid volume Eqs. 55 and 39–41.

6. Steps (3)–(5) are repeated at each time step until the convergence criteria for $T$, $\mathbf{v}$, and $h$ are simultaneously satisfied.

7. Return to step (2) for the next time period.

Convergence criterion for a steady-state is $\left|s^{n+1} - s^n\right|/s^{n+1} < 10^{-3}$, where $s$ is any variable ($u$, $v$, $T$, $h$) at all points and $n$ is the time iteration level. The numerical schemes for both flat and curved free surfaces have been validated in our past work.[24] Property values of steel and nondimensional parameters for numerical simulations are given in Table 1. The $31 \times 31$, $41 \times 41$, $51 \times 51$, and $61 \times 61$ grid systems are used for the grid dependency test, and they have nonuniform grid spacings with denser grids located in the region adjacent to the melt pool. Figure 4 shows the surface temperature and velocity distributions, and the free surface profiles of the melt pool for the flat free surface (Type IV, $V = 1$) with respect to grid size. The errors in the maximum surface temperatures, velocities, and deformations between $51 \times 51$ and $61 \times 61$ grid systems are less than about 3.5%, and the grid-independence is achieved with the $51 \times 51$ grid system, which is used for all computations. The free surface shape is concave (a crater) at the hot center and convex (rim-like) near the cold periphery, because the surface temperature gradient-induced thermocapillary flow drives the molten material toward the cooler region with a higher surface tension.

## Results and Discussion

### *Thermocapillary convection in liquid cylinders*

We have investigated thermocapillary convection for four free surface shapes with $V = 0.8$, $Pr = 30$, $Re = 1000$, and $Ca = 0$ (nondeformable free surfaces). The sets of streamlines and isotherms for the respective free surface shapes are shown in Figure 5. The flow field for other free surface shapes, except for Type III, which has a secondary vortex flow near the hot corner region that is induced by a sharp free surface curvature in both corner regions adjacent to the free surface, is unicellular with a relatively fast outward surface flow from the hot center to the cold wall along the free surface and a return flow toward the hot center. The center of the recirculation cells moves toward the hot center with a change in the free surface shape from Type I to Type II and Type III, and then to Type IV. Thermocapillary convection due to the unicellular flow induces thin thermal boundary layers along the free surface. Large temperature drops occur throughout those boundary layers, so most of the liquid remains relatively cool.

The surface temperature and velocity distributions are shown in Figure 6 using the same conditions as in Figure 5. The surface temperature exhibits a large radial temperature gradient in the region close to the laser beam due to the thin thermal boundary layer along the free surface, and the surface velocity is relatively high in that region. Among the free surface shapes of Types I, II, and IV, as the free surface shape changes from Type I to Type II, and then to Type IV, surface velocities increase due to increased local surface temperature gradients, which are caused by a decrease in the surface temperature near the middle of the free surface. The maximum surface temperature and velocity of Type II are roughly the same as those of Type IV. By contrast, Type I has a significantly higher uniform velocity over the entire free surface than does either Type II or Type IV. This is because a negative radial gradient in the free surface height positively coincides with the flow direction; thus, the flow is

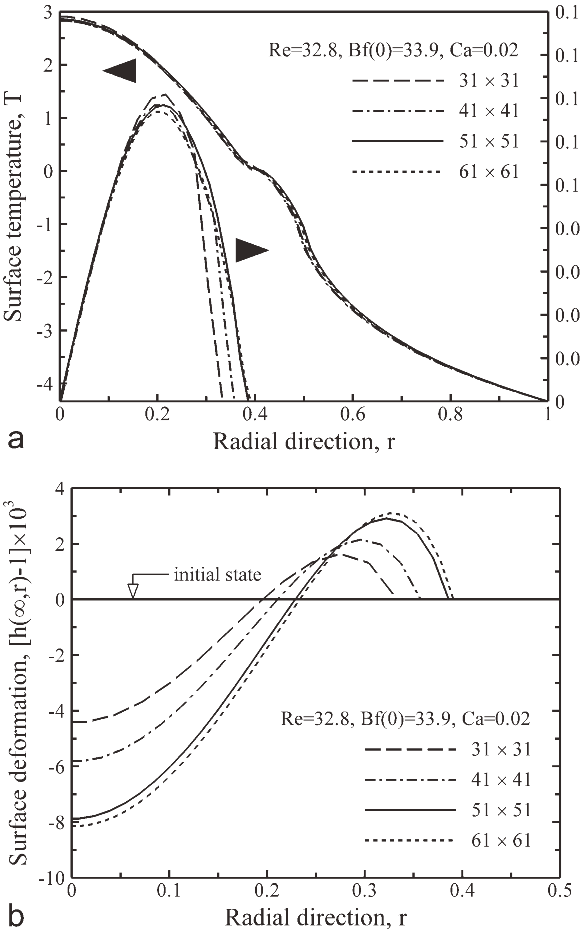

**Figure 4. (a) Surface temperature and velocity distributions, and (b) free surface profiles of the melt pool for a flat surface (Type IV) with four different grids at *Re* = 32.8, *Bf*(0) = 33.9, and *Ca* = 0.02.**

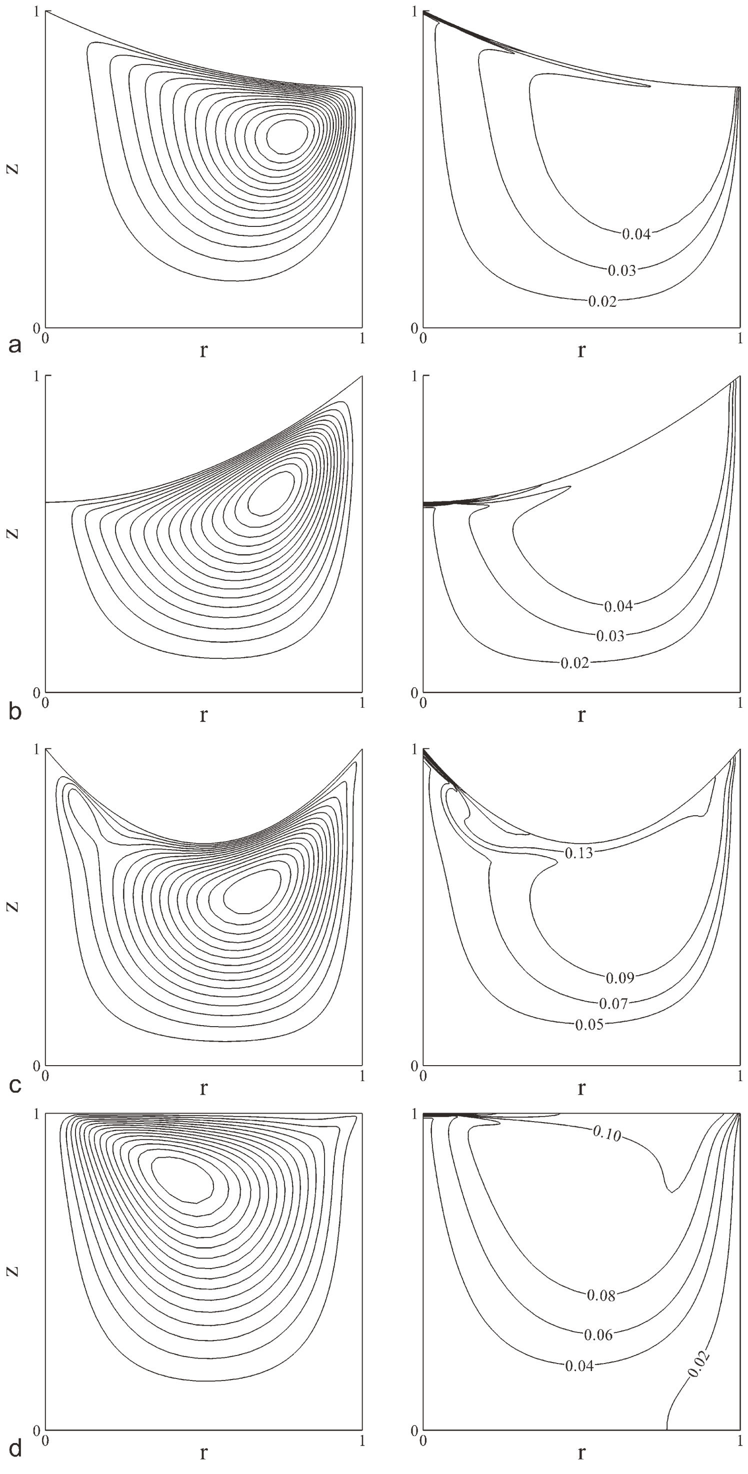

**Figure 5. Streamlines and isotherms with $Re = 1000$, $Pr = 30$, and $H_r = 0.1$ for four surface shapes: (a) Type I, (b) Type II, and (c) Type III with $V = 0.8$, and (d) Type IV with $V = 1$.**

greatly strengthened by the increased inertia forces. In the case of Type III, the surface flow is affected less by the cold return flow due to the secondary vortex flow near the hot corner, as can be seen in Figure 5. This leads to an increase in both the surface temperature along the free surface and the bulk temperature of the liquid. As a result, the surface temperature in the region close to the laser beam are much higher, and those in the rest of the free surface, except for the cold corner, are higher than those of the other free surface shapes, as shown in Figure 6.

The computed maximum stream functions, which represent the overall flow rate, are shown in Figure 7 for four surface shapes and are compared with those in Sim and Zebib[25] for two surface shapes: Types II ($V = 0.81$) and IV ($V = 1$).

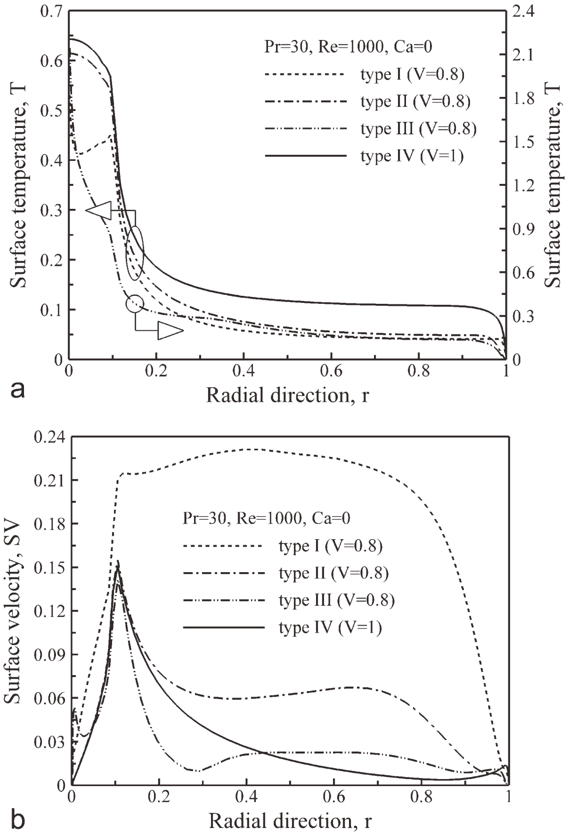

**Figure 6. (a) Surface temperature and (b) velocity distributions corresponding to the four surface shapes in Figure 5.**

As mentioned in the subsection entitled Thermocapillary convection in liquid cylinders in Model Description section, the free surface profile[25] was obtained by solving the Young-Laplace equation with two boundary conditions for a given total fluid volume. The numerical results for both surface shapes agree reasonably well with those in Sim and Zebib.[25] The maximum value of the stream function decreases greatly when varying the surface shape from Type I to Type II and then to Type III, while the maximum stream function of Type III is slightly larger than that of Type IV, but its variation for both Types III and IV is negligible. When the radial slope of the free surface is negative (Type I) or positive (Type II), the maximum stream function is around 11 or three times larger, respectively, than that obtained for the flat surface (Type IV). Accordingly, the above discussion indicates that more vigorous thermocapillary convection in the laser melting process for a fixed workpiece volume can be achieved with the surface shapes of Types I and III compared with those of Types II and IV.

### *Laser melting*

To establish the quantitative correlations between *V* and the melt pool geometry (width, depth, aspect ratio, and volume of the melt pool) as well as the flow (maximum stream function and surface velocity) and thermal (maximum surface temperature) features of the melt pool, two-dimensional numerical simulations of the thermocapillary convection in the laser melting of deformable interfaces are performed with $Re = 32.8$, $Ca = 0.02$, and various *Bf*s for various surface shapes.

Figure 8 shows the surface deformation of the melt pool with respect to *Bf* and *V* for the Type I surface shape. The plus sign on the vertical axis shows that the height of the free surface is greater than that of the initial free surface, while the minus sign indicates the opposite. The flow field in the melt pool shows a large toroidal, single-cell flow, a typical axisymmetric, thermocapillary convection. Compared with the initial free surface, the melt pool surface sinks at the center and rises near the edges of the melt pool because the molten material flows outward from the center. Therefore, at $V < 1$, the free surface of the melt pool becomes flat compared with that of the initial free surface, causing a recovery on the periphery of the melt pool. The shape of the free surface, the number of ripples, and the reflection point do not change with *Bf* and *V*, while the surface deformation, i.e., the magnitudes of depressions and elevations, increases with decreasing *V* at fixed *Bf* because of an attendant increase in the heat energy incident on the top surface beneath the beam and the increased inertia forces of the outward molten material flow, as discussed in the subsection entitled Thermocapillary convection in liquid cylinders in Results and Discussion section. Also, the melt pool widens with an increasing *Bf* and a decreasing *V* at a fixed *V* and *Bf*, respectively. The height of the reflection point near $r = 0.22$ is slightly greater than that of the initial free surface because relatively large amounts of the molten material are carried outward. The order of magnitude of the surface deformation is $O(10^{-2})$. Its maximum value is 0.163, with about 86% of the pool depth at the center, with $Bf(0) = 22.6$ and $V = 0.55$.

With the Type II surface shape, the surface deformations of the molten pool for various *Bf*s and *V*s are shown in Figure 9. As expected, the melt pool width and the surface deformation increase with increasing *Bf* at a fixed *V*. Contrary to the Type I surface shape, the surface deformation and the melt pool width become smaller with decreasing *V* at a fixed *Bf*. As *V* decreases at a fixed *Bf*, the amount of heat

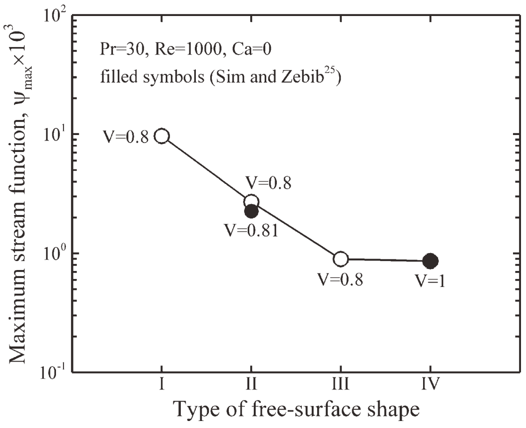

**Figure 7. Maximum stream functions associated with the shapes in Figure 5.**

The filled circle symbol represents the maximum stream functions for two types of surface shapes in Sim and Zebib.[25]

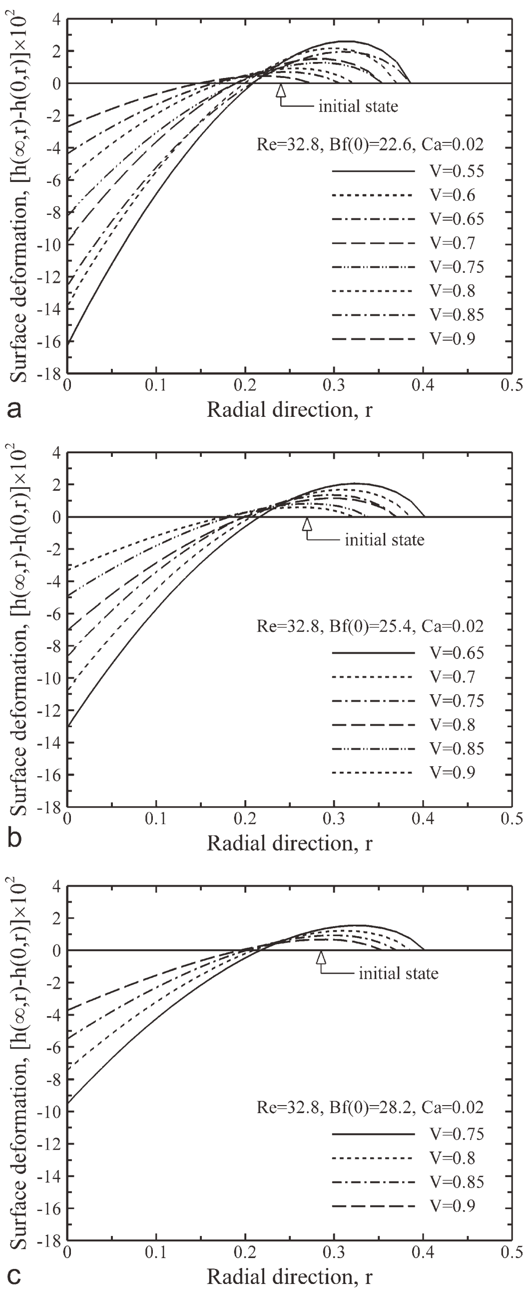

**Figure 8. Free surface deformations of the melt pool with various *Bf*s and *V*s at *Re* = 32.8 and *Ca* = 0.02 for the Type I surface shape: (a) *Bf*(0) = 22.6, (b) *Bf*(0) = 25.4, and (c) *Bf*(0) = 28.2.**

The maximum temperature in the melt pool exceeds the evaporation temperature of the workpiece at *V*s less than 0.55, 0.65, and 0.75 for each *Bf*, so that the surface deformations below the workpiece volumes mentioned above are not presented.

transferred from the bottom and side surfaces to the workpiece by conduction is greater than the slightly increased amount of incident heat on the top surface. Eventually, the enhanced cooling with decreasing $V$ inhibits the formation of the molten pool. The free surface deformation induced by melting is then negligibly small below $V = 0.8$, 0.75, and 0.7 when *Bf*s are 28.2, 33.9, and 39.5, respectively. The free surface forms a bowl-like shape with a deep crater and a low peripheral rim. The surface deformation is $O(10^{-3})$, its maximum value is $1.55 \times 10^{-2}$, about 16% of the pool depth, at the center of the melt pool with $Bf(0) = 39.5$ and $V = 0.9$. At $Bf(0) = 28.2$, the maximum surface deformation with $V = 0.9$ is around 19 times less than that corresponding to the Type I ($V = 0.75$).

Figure 10 shows the variation in surface deformation for various *Bf*s and *V*s with the Type III surface shape. The results show that the surface deformation of the molten pool is almost qualitatively identical to that of Type I, but the surface deformation is significantly greater due to a smaller amount of material near the center and an increase in the incident heat energy compared with that of Type I. The melt pool width is slightly less than that of Type I, especially for smaller *V*s. The free surface profile of the melt pool flattens due to the outward transfer of relatively large amounts of molten material compared with that of the initial free surface. The shape of the free surface, the number of ripples, and the reflection point do not change with workpiece volume, as shown in Figure 10. It is also evident that the height of the reflection point near $r = 0.19$ is slightly greater than that of the initial free surface. The order of magnitude of the surface deformation is $O(10^{-2})$. Its maximum value is 0.205, about 123% of the pool depth, at the center of the melt pool with $Bf(0) = 28.2$ and $V = 0.75$. At $Bf(0) = 28.2$, the maximum surface deformation for $V = 0.75$ is about two and 40 times greater than those of Types I ($V = 0.75$) and II ($V = 0.9$), respectively.

Figure 11 shows the depths and widths of the molten pools for different surface shapes with respect to *Bf* and *V*. As mentioned above, the melt pool widths of Types I and III decrease linearly as $V$ increases, while that of Type II increases. Especially, in the case of Type II at *V*s less than 0.8, 0.75, and 0.7 with $Bf(0) = 28.2$, 33.9, and 39.5, respectively, the melt pool width and depth are negligible mainly due to enhanced cooling. As shown in Figure 11, with $Bf(0) = 28.2$, the slopes of the linear fits for the widths of Types I and III are $-0.29$ and $-0.227$, with intercepts at 0.615 and 0.552, respectively, whereas for Type II the slope is 0.724 with an intercept at $-0.399$. A more detailed description for other operating conditions is available in Table 2. With increasing $V$, the melt pool depths of Types I and III decrease, but that of Type II increases. For the depth of Types I and III at $Bf(0) = 28.2$, the slopes of the linear fits are $-0.345$ and $-0.486$ with intercepts at 0.413 and 0.551, respectively, while the slope for Type II is 0.279 with an intercept at $-0.213$. It is shown that the melt pool widths and depths of Type I are slightly larger and smaller, respectively, than those of Type III.

Figure 12 depicts the melt aspect ratio, defined as the ratio of the depth to the width of the melt pool, with respect to *Bf* and $V$ for various surface shapes. With increasing $V$, the melt aspect ratios of Types I and III decrease, but that of Type II increases. As shown in Figure 11, the aspect ratio of Type III that has less material near the center is greater than that of Type I, and the difference between the two surface types increases with decreasing $V$. At $Bf(0) = 28.2$, the slopes of the linear fits of both Types I and III are $-0.697$ and $-1.193$, with intercepts at 0.912 and 1.398, respectively,

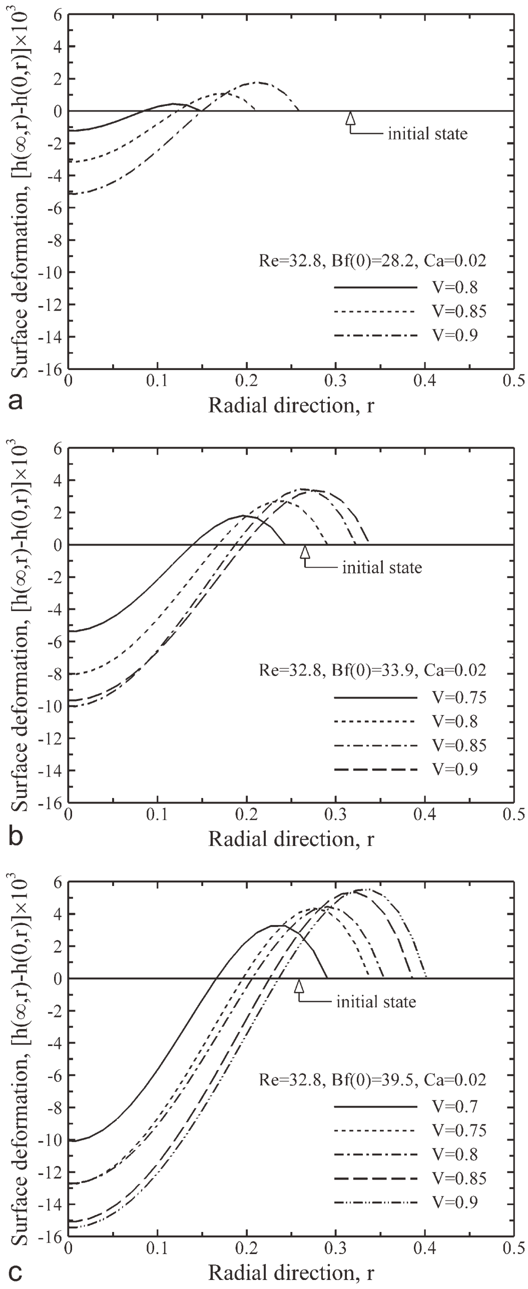

**Figure 9. Free surface deformations of the melt pool with various *Bf*s and *V*s at *Re* = 32.8 and *Ca* = 0.02 for the Type II surface shape: (a) *Bf*(0) = 28.2, (b) *Bf*(0) = 33.9, and (c) *Bf*(0) = 39.5.**

The surface deformation is negligible below $V = 0.8$, 0.75, and 0.7 for each *Bf*, and its profiles are not depicted.

whereas for Type II the slope is 0.638 with an intercept at −0.431.

The effects of *V* and *Bf* on the molten pool volume and the maximum stream function for different surface shapes are presented in Figure 13. Upon increasing *V* at $Bf(0) = 28.2$, the melt pool volumes of both Types I and III decrease, with slopes of $-3.49 \times 10^{-2}$ and $-4.05 \times 10^{-2}$ and intercepts at $3.82 \times 10^{-2}$ and $4.37 \times 10^{-2}$, respectively, while that of Type II increases with a slope of $1.89 \times 10^{-2}$ and an intercept at $-1.56 \times 10^{-2}$. Hence, the convection is more vigorous with decreasing *V* for both Types I and III and with increasing *V* for Type II, as shown in Figure 13. At a fixed *V* smaller than unity (Type IV), the strength of convection becomes greater when the surface shape changes from Type II to Type III and then to Type I. This is because the amount of heat absorbed on the workpiece top surface increases, and the thermocapillary flow is augmented with a greater inertia effect of the outward molten material flow. In the cases of Types I and III with $Bf(0) = 28.2$, the slopes of the linear fits are $-4.05 \times 10^{-3}$ and $-6 \times 10^{-3}$ with

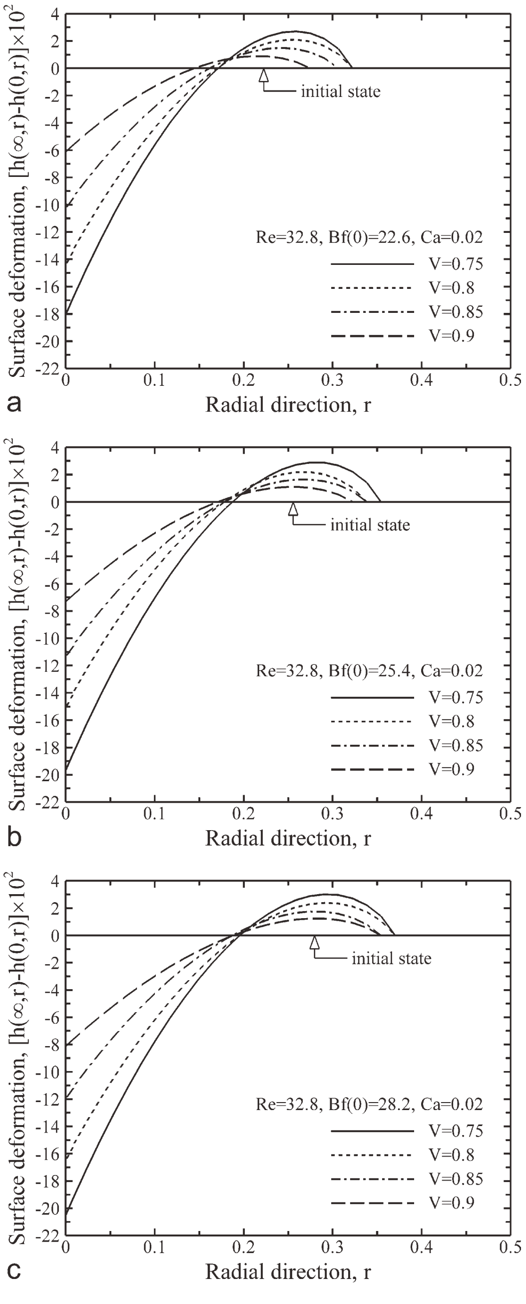

**Figure 10. Free surface deformations of the melt pool with various *Bf*s and *V*s at *Re* = 32.8 and *Ca* = 0.02 for the Type III surface shape: (a) *Bf*(0) = 22.6, (b) *Bf*(0) = 25.4, and (c) *Bf*(0) = 28.2.**

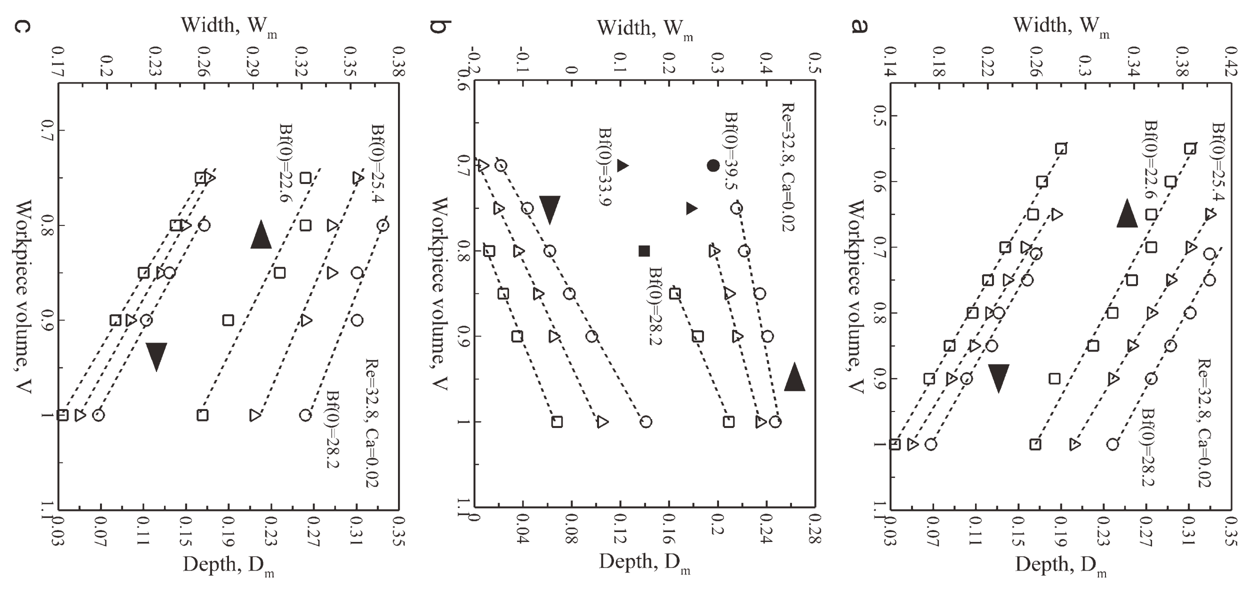

**Figure 11. Depths and widths of the melt pool vs. *V* for various surface shapes and *Bf*s (*Re* = 32.8 and *Ca* = 0.02): (a) Type I, (b) Type II, and (c) Type III.**

The dashed line shows a linear fit of the melt pool width and depth depending on *V* for the different surface shapes and *Bf*s. For the Type II pool width, the filled symbol data below *V* = 0.85, 0.8, and 0.75 for each *Bf* are excluded from the correlation analysis because of enhanced cooling.

intercepts at $4.07 \times 10^{-3}$ and $6.04 \times 10^{-3}$, respectively, while the slope for Type II is $3.66 \times 10^{-4}$ with an intercept at $-3.09 \times 10^{-4}$. In particular, when *Bf* is relatively small (less than 28.2), the flow in the melt pool becomes stronger with a decreasing *V* less than 0.75 and 0.85 for Types I and III, respectively. The increments of the flow strength below

**Table 2. The Correlation Coefficients ($c_1$, $c_2$) and the Applicable Ranges of the Linear Fits shown in Figures 11−14**

| Type | *Bf*(0) | $D_m$ | $W_m$ | $D_m/W_m$ | $V_m$ | $\psi_{max}$ | $T_{max}$ | $SV_{max}$ |
|---|---|---|---|---|---|---|---|---|
| I | 22.57 | −0.353, 0.386<br>($V \geq 0.55$) | −0.288, 0.547<br>($V \geq 0.55$) | −0.801, 0.955<br>($V \geq 0.55$) | −0.0326, 0.032<br>($V \geq 0.55$) | −0.00505, 0.00408 ($0.55 \leq V \leq 0.7$)<br>−0.00188, 0.00183 ($V > 0.7$) | −7.31, 7.877<br>($V \geq 0.55$) | −0.723, 0.736<br>($V \geq 0.55$) |
| | 25.39 | −0.372, 0.422<br>($V \geq 0.65$) | −0.318, 0.609<br>($V \geq 0.65$) | −0.782, 0.967<br>($V \geq 0.65$) | −0.0374, 0.0382<br>($V \geq 0.65$) | −0.00674, 0.00576 ($0.65 \leq V \leq 0.75$)<br>−0.00273, 0.00271 ($V > 0.75$) | −8.149, 9.178<br>($V \geq 0.65$) | −0.933, 0.969<br>($V \geq 0.65$) |
| | 28.21 | −0.345, 0.413<br>($V \geq 0.71$) | −0.29, 0.615<br>($V \geq 0.71$) | −0.697, 0.912<br>($V \geq 0.71$) | −0.0349, 0.0382<br>($V \geq 0.71$) | −0.00405, 0.00407 ($V \geq 0.55$) | −7.758, 9.43<br>($V \geq 0.71$) | −1.068, 0.99<br>($V \geq 0.71$) |
| II | 28.21 | 0.279, −0.213<br>($V \geq 0.8$) | 0.724, −0.399<br>($V \geq 0.85$) | 0.638, −0.431<br>($V \geq 0.8$) | 0.0189, −0.0156<br>($V \geq 0.85$) | 0.000366, −0.000309 ($V \geq 0.85$) | 6.87, −5.273<br>($V \geq 0.8$) | 0.299, −0.233<br>($V \geq 0.8$) |
| | 33.85 | 0.324, −0.223<br>($V \geq 0.7$) | 0.463, −0.077<br>($V \geq 0.8$) | 0.707, −0.441<br>($V \geq 0.7$) | 0.0292, −0.0219<br>($V \geq 0.8$) | 0.00129, −0.00101 ($V \geq 0.8$) | 8.851, −6.024<br>($V \geq 0.7$) | 0.604, −0.427<br>($V \geq 0.7$) |
| | 39.49 | 0.388, −0.249<br>($V \geq 0.7$) | 0.332, 0.0943<br>($V \geq 0.75$) | 0.84, −0.508<br>($V \geq 0.7$) | 0.0376, −0.254<br>($V \geq 0.8$) | 0.0029, −0.00214 ($V \geq 0.75$) | 10.25, −6.214<br>($V \geq 0.7$) | 1.066, −0.718<br>($V \geq 0.7$) |
| III | 22.57 | −0.524, 0.557<br>($V \geq 0.75$) | −0.287, 0.544<br>($V \geq 0.75$) | −1.485, 1.625<br>($V \geq 0.75$) | −0.0336, 0.0338<br>($V \geq 0.75$) | −0.00529, 0.00483 ($0.75 \leq V \leq 0.85$)<br>−0.00227, 0.00227 ($V > 0.85$) | −11.121, 11.688<br>($V \geq 0.75$) | −1.227, 1.246<br>($V \geq 0.75$) |
| | 25.39 | −0.491, 0.541<br>($V \geq 0.75$) | −0.245, 0.539<br>($V \geq 0.75$) | −1.276, 1.451<br>($V \geq 0.75$) | −0.0391, 0.0404<br>($V \geq 0.75$) | −0.00744, 0.00688 ($0.75 \leq V \leq 0.85$)<br>−0.00351, 0.00352 ($V > 0.85$) | −11.751, 12.778<br>($V \geq 0.75$) | −1.489, 1.521<br>($V \geq 0.75$) |
| | 28.21 | −0.486, 0.551<br>($V \geq 0.8$) | −0.227, 0.552<br>($V \geq 0.8$) | −1.193, 1.398<br>($V \geq 0.8$) | −0.0405, 0.0437<br>($V \geq 0.8$) | −0.006, 0.00604 ($V \geq 0.8$) | −11.434, 13.036<br>($V \geq 0.8$) | −1.672, 1.731<br>($V \geq 0.8$) |

The workpiece volumes in parentheses indicate the applicable ranges of the correlations obtained, where the linear fits for various parameters are expressed as $c_1V + c_2$.

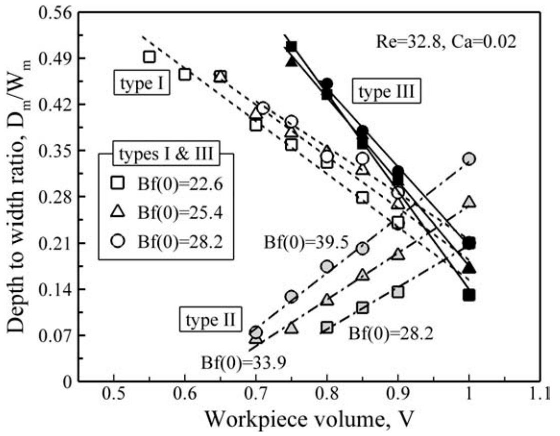

**Figure 12. Depth to width ratios of the melt pool vs. *V* for various surface shapes and *Bf*s at *Re* = 32.8 and *Ca* = 0.02.**

The line depicts the linear fit of the ratio of the depth to the width of the melt pool depending on *V* for different surface shapes and *Bf*s.

$V = 0.75$ (Type I) and 0.85 (Type III) are about 2.6 and 2.2 times higher, respectively, than that above each *V*.

The maximum surface temperature and velocity in the melt pool with respect to *Bf* and *V* for various surface shapes are shown in Figure 14. The maximum temperature and velocity on the free surface of the melt pool increase with increasing *Bf*, regardless of the surface shape or *V* of the workpiece. Upon increasing *V* at a fixed *Bf*, the maximum temperatures and velocities of Types I and III decrease, while those of Type II increase. For the maximum temperatures of Types I and III with $Bf(0) = 28.2$, the slopes of the linear fits are $-7.758$ and $-11.434$ with intercepts at 9.43 and 13.036, respectively, while the slope for Type II is 6.87 with an intercept at $-5.273$. In the case of the maximum velocity with $Bf(0) = 28.2$, the slopes of the linear fits of both Types I and III are $-1.068$ and $-1.672$ with intercepts at 0.99 and 1.731, respectively, but for Type II, the slope is 0.299 with an intercept at $-0.233$.

It is well known that steady, axisymmetrical thermocapillary flow becomes unstable and oscillatory three-dimensional flow states develop.[32,33] However, flow instabilities are not investigated in this study because of their three-dimensional natures. The instability of thermocapillary convection in an open cylinder with a uniform heat flux can be found in Sim and Zebib.[25]

## Conclusions

The aim of this article was to establish quantitative correlations between *V* and melt pool geometry (width, depth, aspect ratio, and volume of the melt pool) as well as the flow (maximum stream function and surface velocity) and thermal (maximum surface temperature) features of the melt pool under different low-power laser intensities for various surface shapes. Prior to solving the laser melting problems, two-dimensional numerical simulations were performed to examine the effect of the free surface shape on the flow characteristics of thermocapillary convection driven by a uniform heat flux in an open cylinder of unit aspect ratio with a nondeformable free surface. Then, axisymmetric thermocapillary convection in laser melting with a Gaussian heat flux was investigated to analyze how the shape, size, and surface topography of the melt pool with deformable interfaces were affected by surface shape and *V*.

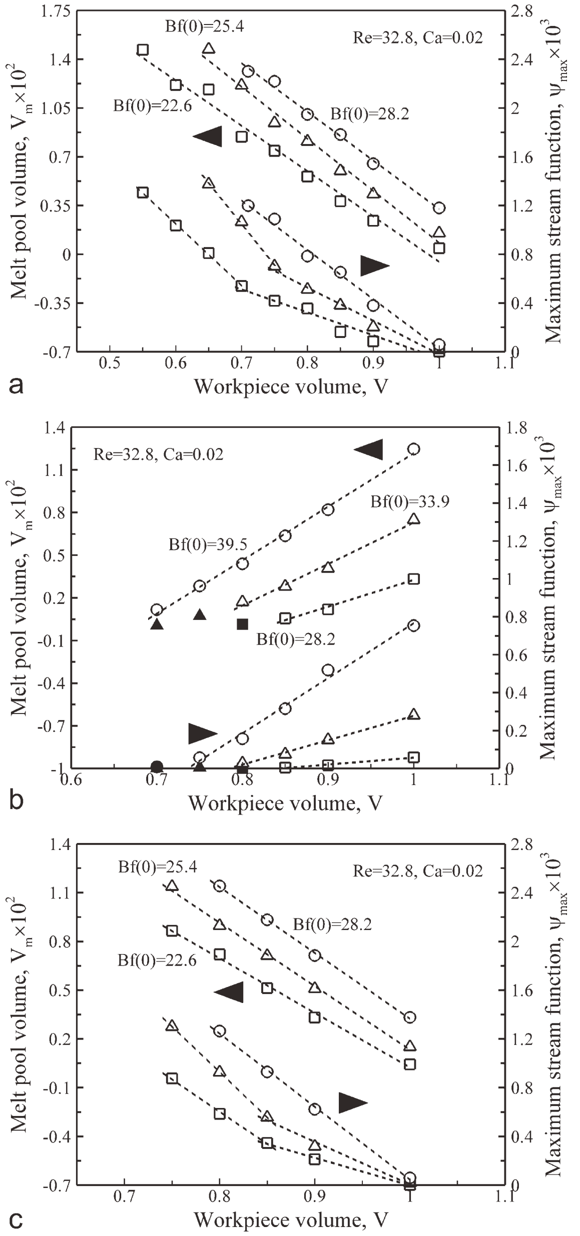

**Figure 13. Melt pool volumes and maximum stream functions vs. *V* for various surface shapes and *Bf*s at *Re* = 32.8 and *Ca* = 0.02: (a) Type I, (b) Type II, and (c) Type III.**

The dashed line represents the linear fit of the melt pool volume and maximum stream function depending on *V* for different surface shapes and *Bf*s. For the Type II melt pool volume with $Bf(0) = 28.2$ and 33.9, the filled symbol data below $V = 0.85$ and 0.8, respectively, are excluded from the correlation analysis.

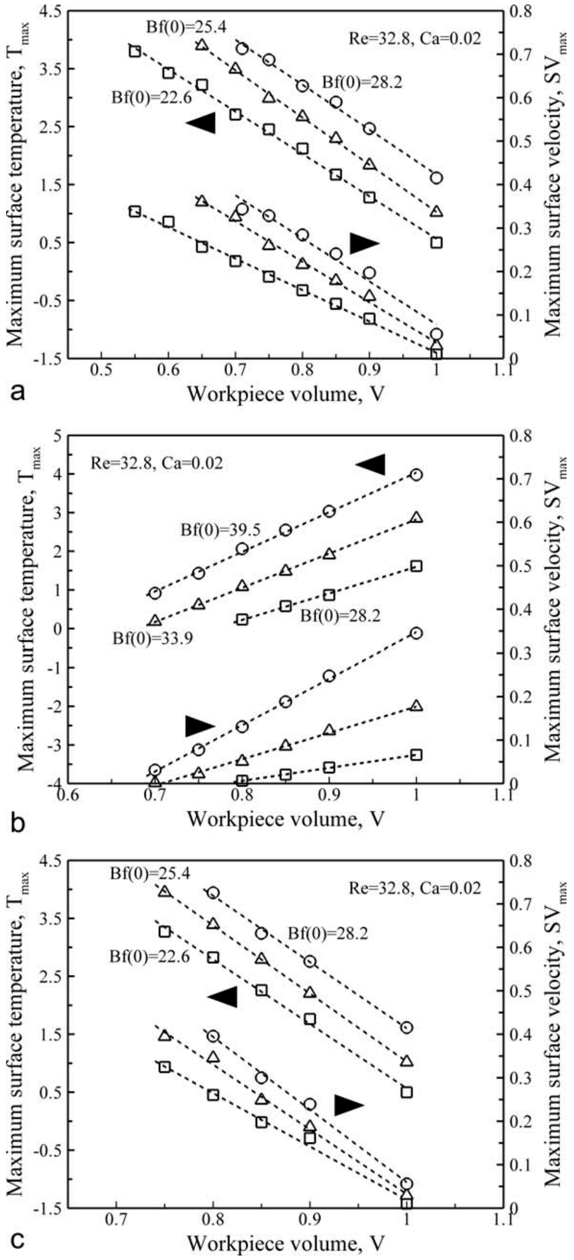

**Figure 14. Maximum surface temperatures and velocities vs. *V* for various surface shapes and *Bf*s at *Re* = 32.8 and *Ca* = 0.02: (a) Type I, (b) Type II, and (c) Type III.**

The dashed line indicates the linear fit of the maximum surface temperature and velocity depending on $V$ for different surface shapes and $Bf$s.

The free surface of the melt pool at steady-state sunk at the center and rose near the edges of the molten pool due to the outward motion of the molten material. For both Types I and III, the free surfaces flattened due to the outward transfer of relatively large amounts of molten material compared with that of the initial free surface. The surface deformation increased with decreasing $V$ at a fixed $Bf$, because the heat energy incident on the top surface beneath the beam increased, and the inertia forces of the outward molten material flow were enhanced. By contrast, the free surfaces of both Types II and IV formed bowl-like shapes with deep craters and low peripheral rims. Hence, the surface deformation decreased with decreasing $V$ at a fixed $Bf$ because of the enhanced cooling. Upon increasing $V$ at a fixed $Bf$, the width, depth, aspect ratio, and volume of the melt pool, as well as the maximum stream functions, surface velocities, and temperatures for both Types I and III all decreased linearly. For Type II, these values increased linearly.

In this study, thermocapillary convection during laser melting was not considered for operating conditions in which the maximum temperature in the melt pool exceeded the evaporation temperature of the workpiece. Therefore, future work is required to clarify the effect of surface shape on the geometric, flow, and thermal characteristics of the melt pool above the evaporation temperature of the workpiece under high-power laser intensity.

## Notation

$a$, $b$ = coefficients in the free surface shape functions
$Bf$ = boundary heating factor, $q''r_bC_p/k_1\lambda$
$c_1$, $c_2$ = correlation coefficient of the linear fit
$C_a$ = Capillary number, $\gamma T_r/\sigma_0$ in Eq. 10, $\gamma\lambda/\sigma_0 C_p$ in Eq. 37
$C_p$ = specific heat, J kg$^{-1}$ K$^{-1}$
$c(t)$ = free integration constant
$D$ = height of the cylinder and workpiece or dimensionless melt pool depth
$f$ = liquid fraction
$H$ = dimensionless enthalpy
$h$ = dimensionless free surface height
$k$ = dimensionless thermal conductivity
$Ma$ = Marangoni number, $PrRe$
$P$ = dimensionless pressure
$Pr$ = Prandtl number, $\nu/\alpha$
$Q$ = heat rate, W
$q$ = dimensionless heat flux
$q''$ = laser heat flux, $3\phi Q/\pi r_b^2\exp(-3r^2/r_b^2)$, W m$^{-2}$
$q_0$* = average heat flux, $Q/\pi R^2$, W m$^{-2}$
$R$ = radius of the cylinder and workpiece, m
$r$ = radial coordinate
$r_b$ = radius of the laser beam, m
$Re$ = Reynolds number, $\gamma T_r D/\nu\mu$ in Eq. 3, $U_R r_b/\nu$ in Eq. 29
$r_{max}$ = dimensionless melt pool width
$\mathbf{S}$ = source term vector
$Ste$ = Stefan number, $C_p(T_m-T_\infty)/\lambda$
$SV$ = dimensionless surface velocity, $(u^2 + \upsilon^2)^{0.5}$
$T$ = dimensionless temperature
$t$ = dimensionless time
$T_m$ = melting temperature, K
$T_r$ = characteristic $T$, $q_0{*}D/k$
$u$ = dimensionless radial velocity
$U_R$ = surface tension reference velocity, $\gamma\lambda/C_p\mu$
$V$ = dimensionless volume of the liquid and workpiece
$\mathbf{v}$ = dimensionless velocity vector
$\upsilon$ = dimensionless axial velocity
$V_m$ = dimensionless volume of the melt pool
$W$ = dimensionless melt pool width
$z$ = axial coordinate

### *Greek letters*

$\lambda$ = latent heat of fusion, J kg$^{-1}$
$\nu$ = kinematic viscosity, m$^2$ s$^{-1}$
$\mu$ = dynamic viscosity, N s m$^{-2}$
$\alpha$ = thermal diffusivity, m$^2$ s$^{-1}$
$\gamma$ = $-\partial\sigma/\partial T$, N m$^{-1}$ K$^{-1}$
$\rho$ = density, kg m$^{-3}$
$\sigma$ = surface tension, N m$^{-1}$

$\phi$ = adsorption coefficient
$\psi$ = dimensionless stream function

### Subscripts

1 = liquid
m = melt pool
max = maximum
s = solid
0 = reference state
$\infty$ = ambient

### Superscripts

* = dimensional quantity

## Literature Cited

1. Sandven OA. Laser Surface Hardening. In: *ASM Handbook*, Materials Park, OH: ASM International, 1991;4:286–296.
2. Baumgart P, Krajnovich DJ, Nguyen TA, Tam AC. A new laser texturing technique for high performance magnetic of Ni-P disks. *IEEE Trans Magn.* 1995;31:2946–2951.
3. Chen SC, Grigoropoulos CP, Park HK, Kerstens P, Tam AC. Photothermal displacement detection and transient imaging of bump dynamics in laser zone texturing of Ni-P disk substrates. *J Appl Phys.* 1999;85:5619–5620.
4. Chen SC, Cahill DG, Grigoropoulos CP. Melting and surface deformation in pulsed laser surface micromodification of Ni-P disks. *J Heat Transfer.* 2000;122:107–112.
5. Willis DA, Xu X. Transport phenomena and droplet formation during pulsed laser interaction with thin films. *J Heat Transfer.* 2000; 122:763–770.
6. Bin-Mansoor S, Yilbas BS. Laser pulse heating of steel surface: consideration of phase-change process. *Numer Heat Transfer A.* 2006; 50:787–807.
7. Yilbas BS, Shuja SZ, Khan SMA, Aleem A. Laser melting of carbide tool surface: model and experimental studies. *Appl Surf Sci.* 2009;255:9396–9403.
8. Li JF, Li L, Stott FH. Predictions of flow velocity and velocity boundary layer thickness at the surface during laser melting of ceramic materials. *J Phys D: Appl Phys.* 2004;37:1710–1717.
9. Srinivasan J, Basu B. A numerical study of thermocapillary flow in a rectangular cavity during laser melting. *Int J Heat Mass Transfer.* 1986;29:563–573.
10. Chan CL, Mazumder J, Chen MM. Effect of surface tension gradient driven convection in a laser melt pool: three-dimensional perturbation model. *J Appl Phys.* 1988;64:6166–6174.
11. Basu B, Date AW. Numerical study of steady state and transient laser melting problems. I. Characteristics of flow field and heat transfer. *Int J Heat Mass Transfer.* 1990;33:1149–1163.
12. Ravindran K, Srinivasan J, Marathe AG. Finite element study on the role of convection in laser surface melting. Numer Heat Transfer A. 1994;26:601–618.
13. Kim W-S, Sim B-C. Study of thermal behavior and fluid flow during laser surface heating of alloys. Numer Heat Transfer A. 1997;31:703–723.
14. Chakraborty N, Chatterjee D, Chakraborty S. A scaling analysis of turbulent transport in laser surface alloying process. *J Appl Phys.* 2004;96:4569–4577.
15. Wang H-X, Cheng K, Chen X, Pan W. Three-dimensional modeling of heat transfer and fluid flow in laminar-plasma material re-melting processing. *Int J Heat Mass Transfer.* 2006;49:2254–2264.
16. Chakraborty N, Chakraborty S. Modelling of turbulent molten pool convection in laser welding of a copper-nickel dissimilar couple. *Int J Heat Mass Transfer.* 2007;50:1822–1822.
17. Safdar S, Li L, Sheikh MA. Numerical analysis of the effects of non-conventional laser beam geometries during laser melting of metallic materials. *J Phys D: Appl Phys.* 2007;40:593–603.
18. Iwamoto M, Ye M, Grigoropoulos CP, Greif R. Numerical analysis of pulsed laser heating for the deformation of metals. Numer Heat Transfer A. 1998;34:791–804.
19. Ajaev VS, Willis DA. Thermocapillary flow and rupture in films of molten metal on a substrate. *Phys Fluids.* 2003;15:3144–3150.
20. Han L, Liou FW. Numerical investigation of the influence of laser beam mode on melt pool. *Int J Heat Mass Transfer.* 2004;47:4385–4402.
21. Ha E-J, Kim W-S. A study of low-power density laser welding process with evolution of free surface. *Int J Heat Fluid Flow.* 2005; 26:613–621.
22. Han L, Liou FW, Musti S. Thermal behavior and geometry model of melt pool in laser material process. *J Heat Transfer.* 2005;127: 1005–1014.
23. Sim B-C, Kim W-S. Melting and dynamic-surface deformation in laser surface heating. *Int J Heat Mass Transfer.* 2005;48: 1137–1144.
24. Kim Y-D, Kim W-S. A numerical analysis of heat and fluid flow with a deformable curved free surface in a laser melting process. *Int J Heat Fluid Flow.* 2008;29:1481–1493.
25. Sim B-C, Zebib A. Thermocapillary convection with undeformable curved surfaces in open cylinders. *Int J Heat Mass Transfer.* 2002;45:4983–4994.
26. Mundrane M, Zebib A. Low Prandtl number Marangoni convection with a deformable interface. *AIAA J Thermophys Heat Transfer.* 1995;9:795–797.
27. Broyden CG. A class of methods for solving nonlinear simultaneous equations. *Math Comput.* 1965;19:577–593.
28. Kamotani Y, Ostrach S, Pline A. A thermocapillary convection experiment in microgravity. *J Heat Transfer.* 1995;117:611–618.
29. Li JF, Li L, Stott FH. Comparison of volumetric and surface heating sources in the modeling of laser melting of ceramic materials. *Int J Heat Mass Transfer.* 2004;47:1159–1174.
30. Hector LG, Hetnarski RB. Thermal stresses in materials due to laser heating. *Therm Stresses.* 1996;4:453–531.
31. Swaminathan CR, Voller VR. On the enthalpy method. *Int J Numer Meth Heat Fluid Flow.* 1993;3:233–244.
32. Schwabe D, Zebib A, Sim B-C. Oscillatory thermocapillary convection in open cylindrical annuli. Part 1. Experiments under microgravity. *J Fluid Mech.* 2003;491:239–258.
33. Sim B-C, Zebib A, Schwabe D. Oscillatory thermocapillary convection in open cylindrical annuli. Part 2. Simulations. *J Fluid Mech.* 2003;491:259–274.

*Manuscript received Dec. 8, 2010, and revision received Mar. 9, 2011.*